

# Modulus–density scaling behaviour and framework architecture of nanoporous self-assembled silicas

HONGYOU FAN<sup>1,2</sup>, CHRISTOPHER HARTSHORN<sup>2</sup>, THOMAS BUCHHEIT<sup>1</sup>, DAVID TALLANT<sup>1</sup>,  
ROGER ASSINK<sup>1</sup>, REGINA SIMPSON<sup>1</sup>, DAVE J. KISSEL<sup>2</sup>, DANIEL J. LACKS<sup>3</sup>, SALVATORE TORQUATO<sup>4</sup>  
AND C. JEFFREY BRINKER<sup>1,2\*</sup>

<sup>1</sup>Sandia National Laboratories, Advanced Materials Laboratory, 1001 University Blvd SE, Albuquerque, New Mexico 87106, USA

<sup>2</sup>The University of New Mexico/NSF Center for Micro-Engineered Materials and Department of Chemical and Nuclear Engineering, Albuquerque, New Mexico 87131, USA

<sup>3</sup>Case Western Reserve University, Department of Chemical Engineering, Cleveland, Ohio 44106, USA

<sup>4</sup>Princeton University, Department of Chemistry and Princeton Institute for the Science and Technology of Materials, Princeton, New Jersey 08544, USA

\*e-mail: cjbrink@sandia.gov

Published online: 21 May 2007; doi:10.1038/nmat1913

Natural porous materials such as bone, wood and pith evolved to maximize modulus for a given density<sup>1</sup>. For these three-dimensional cellular solids, modulus scales quadratically with relative density<sup>2,3</sup>. But can nanostructuring improve on Nature's designs? Here, we report modulus–density scaling relationships for cubic (C), hexagonal (H) and worm-like disordered (D) nanoporous silicas prepared by surfactant-directed self-assembly. Over the relative density range, 0.5 to 0.65, Young's modulus scales as (density)<sup>*n*</sup> where  $n_{(C)} < n_{(H)} < n_{(D)} < 2$ , indicating that nanostructured porous silicas exhibit a structure-specific hierarchy of modulus values  $D < H < C$ . Scaling exponents less than 2 emphasize that the moduli are less sensitive to porosity than those of natural cellular solids, which possess extremal moduli based on linear elasticity theory<sup>4</sup>. Using molecular modelling and Raman and NMR spectroscopy, we show that uniform nanoscale confinement causes the silica framework of self-assembled silica to contain a higher portion of small, stiff rings than found in other forms of amorphous silica. The nanostructure-specific hierarchy and systematic increase in framework modulus we observe, when decreasing the silica framework thickness below 2 nm, provides a new ability to maximize mechanical properties at a given density needed for nanoporous materials integration<sup>5</sup>.

Many natural cellular solids exhibit a quadratic scaling relationship between modulus and density:

$$\text{Cellular solids: } (E/E_s) \sim (\rho/\rho_s)^2, \quad (1)$$

where  $E$  is Young's modulus,  $\rho$  is density and the subscript  $s$  denotes the respective property value of the non-porous solid framework. Figure 1a shows that this relationship holds for open-cell bone over a wide range of density. The scaling exponent  $n = 2$  is attributed to the bending moment of the struts comprising the cell walls<sup>3</sup>, and linear-elastic analysis of bone has shown it to be nearly optimal or 'extremal' (yielding the highest modulus for a given density, corresponding to a Hashin–Shtrikman (H–S) upper bound<sup>4</sup>).

Such optimized designs have been emulated in synthetic porous materials such as foamed polymers, ceramics and metals, resulting in similar scaling behaviours<sup>3</sup>. However, foaming processes are limited to cell sizes greater than about 0.1 μm. To achieve the much smaller (0.4–50 nm) pore sizes needed for ceramic thin-film applications such as membranes, molecular recognition sensors and low- $k$  dielectrics (low-dielectric-constant insulators needed for future generations of microelectronic devices), sol–gel processing techniques<sup>5</sup> have been used. Highly porous dried gels (aerogels or xerogels) are normally described by a mass fractal dimension and show a much steeper power-law scaling relationship<sup>6</sup> (see Fig. 1a):

$$\text{Highly porous gels: } (E/E_s) \sim (\rho/\rho_s)^{3.6}. \quad (2)$$

The distinction is that unlike cellular solids, highly porous gels are not completely mechanically connected, so densification causes a progressively greater portion of the structure to become load bearing as dangling arms impinge on one another.

A consequence of relationships (1) and (2) is that for gels and even optimized cellular solids, the modulus is reduced appreciably by the introduction of porosity. This is very problematic for the integration of nanoporous materials into thin-film devices, such as low- $k$  dielectrics<sup>7,8</sup>, where it is desirable to increase porosity (reduce  $k$ ) for successive generations without suffering a dramatic reduction in mechanical properties<sup>8</sup>. Recently, silica/surfactant self-assembly procedures have been developed to create highly ordered, nanoporous thin films<sup>9</sup> with  $k$  values ranging from 2.5 to 1.5 (ref. 10), spanning those needed for the next several generations of microelectronics over which the effective  $k$  will be reduced from 3.4 to as low as 1.6. Although there have been several reports of the mechanical stability<sup>11–13</sup> and modulus<sup>14</sup> of surfactant-templated and polymer-templated materials<sup>15</sup> prepared at a specific density, here we report the modulus as a function of density. Establishment of the modulus–density scaling relationship for this new class of nanostructured materials is important for integration as well as understanding fundamentally how nanostructuring

influences the silica framework architecture and density-dependent mechanical properties compared with other conventional forms of amorphous silica.

Porous silica films with isotropic worm-like disordered (D), two-dimensional (2D) hexagonal (H) or primitive cubic (C), nanostructures were prepared on single-crystal silicon (100) substrates by an evaporation-induced self-assembly procedure<sup>9,16</sup>. We varied the surfactant (Brij-56,  $\text{CH}_3(\text{CH}_2)_{15}(\text{OC}_2\text{H}_4)_{10}\text{OH}$ ) molar concentration from 0.037 to 0.074 M to achieve three different relative densities and designed ageing and calcination conditions to develop D, H or C mesophases (from identical parent films) at each value of the relative density, while maintaining equivalent extents of siloxane condensation (about 93% as determined by <sup>29</sup>Si NMR, see following discussion). Grazing-incidence and symmetric-reflection small-angle X-ray scattering (GISAXS and SRSAXS)<sup>17</sup> and transmission electron microscopy (TEM) were used to characterize the film structure. Volume-fraction porosity, determined from refractive index and surface-acoustic-wave-based nitrogen sorption experiments<sup>18</sup>, was used to calculate the film density. We carried out nanoindentation experiments to determine the reduced indentation modulus,  $E_r$ , which is related to Young's modulus<sup>19</sup>,  $E$ , as  $E_r = E(1 - \nu^2)$ , where  $\nu$  is Poisson's ratio.

Figure 2 shows cross-sectional and plan-view TEM images of the D, H and C films. As denoted by the worm-like texture (Fig. 2a), D films are isotropic with entangled, uniform, cylindrical pores. H films consist of cylindrical pores organized into hexagonally ordered domains with cylinder axes oriented parallel to the substrate surface (appearing as stripes in the cross-sectional image in Fig. 2b). The plan-view TEM image (Fig. 2b, inset) shows swirling patterns resulting from bending of these domains within the plane of the film. C films exhibit 3D periodic order (Fig. 2c). The square pattern observed in plan-view (Fig. 2c, inset) is consistent with a (100)-oriented cubic unit cell.

Figure 1b shows the logarithm of Young's modulus versus the logarithm of bulk density for the C, H and D nanostructured films. We note two key features. First, for all densities there exists a hierarchy of Young's moduli:  $E_C > E_H > E_D$ . Second, each of the self-assembled nanostructures exhibits a different scaling behaviour characterized by scaling exponents,  $n_C = 0.6 < n_H = 1.0 < n_D = 1.9$ .  $n < 2$  indicates that the elastic moduli of the nanostructured silicas are less sensitive to porosity than those of natural cellular solids. Because, on the scale of the nanoindentation experiment, the nanostructured silicas behave linear-elastically, we expect the H-S bounds to apply. Using the H-S bounds of two-phase isotropic materials<sup>4</sup>, we can show rigorously that the anomalous scaling ( $n < 2$ ) we observe for the cubic nanostructure is consistent with a density-dependent framework modulus that increases with increasing porosity/decreasing density (see the Supplementary Information). We note further that the measured Young's modulus values for C, H and D films ( $\sim 10$ –20 GPa, see Supplementary Information) exceed those of comparable sintered sol-gel silica films and other candidate amorphous and polymeric low- $k$  materials<sup>20</sup>. For example,  $E$  for film C prepared with density  $1.1 \text{ g cm}^{-3}$  and dielectric constant 2.42 (ref. 21) equals 18.5 GPa compared with  $\sim 10$  GPa for the corresponding sintered sol-gel film<sup>20</sup>.

To elucidate the physics underlying the unusually weak dependence of Young's modulus on density, we carried out molecular simulations of nanostructured amorphous silica slabs as the slab thickness was reduced from 2.0 to about 1.0 nm, values spanning the range of wall thicknesses deduced for Brij-56- and Brij-58-templated films by analysis of GISAXS and X-ray reflectivity data<sup>17</sup>. The simulations (Fig. 3) show that the atomic-level structure and mechanical properties of nanoconfined

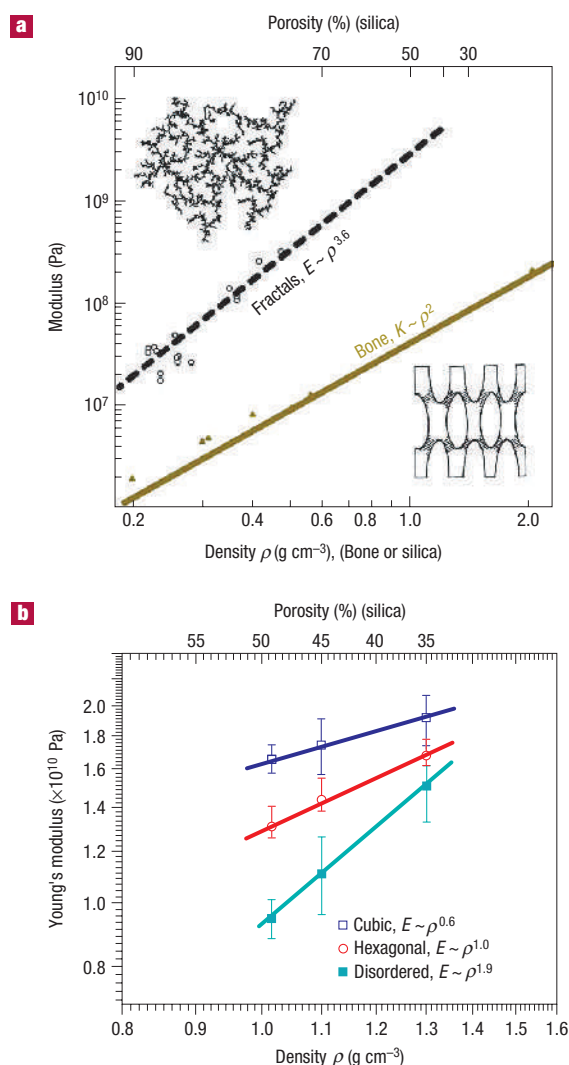


**Figure 1** Modulus–density scaling relationships. **a**, Logarithm modulus versus logarithm bulk density for porous gels and bone. The scaling relationships of gels and human bone are described by  $E \sim \rho^{3.6}$  and  $K \sim \rho^2$ , respectively. Left inset: Simulated fractal architecture. Right inset: Schematic diagram of cellular architecture representative of bone. **b**, Logarithm of Young's modulus versus logarithm of bulk density for self-assembled thin-film nanostructures C, H and D determined by nanoindentation. The power-law relationships of C, H and D films are  $E \sim \rho^{0.6}$ ,  $E \sim \rho^{1.0}$  and  $E \sim \rho^{1.9}$ , respectively. Modulus values were determined at a constant depth (less than 1/10 of the film thickness) where the modulus versus depth values were constant. This procedure should ensure modulus values comparable to bulk values<sup>18</sup>. Young's modulus was calculated from the nanoindentation modulus according to  $E_r = E(1 - \nu^2)$ , where  $E$  is Young's modulus and  $\nu$  is Poisson's ratio. The standard deviation was determined from the mean of ten measurements.

silica differ markedly from those of bulk amorphous silica and change as the size of the confinement changes.

Most importantly, we observe that decreasing slab thickness causes a monotonic increase in Young's modulus and density brought about by changes in the atomic-scale structure. With decreasing slab thickness, there is a progressive reduction in the average siloxane ring size and Si–O–Si bond angle owing to an increase in the concentrations of three- and four-membered rings

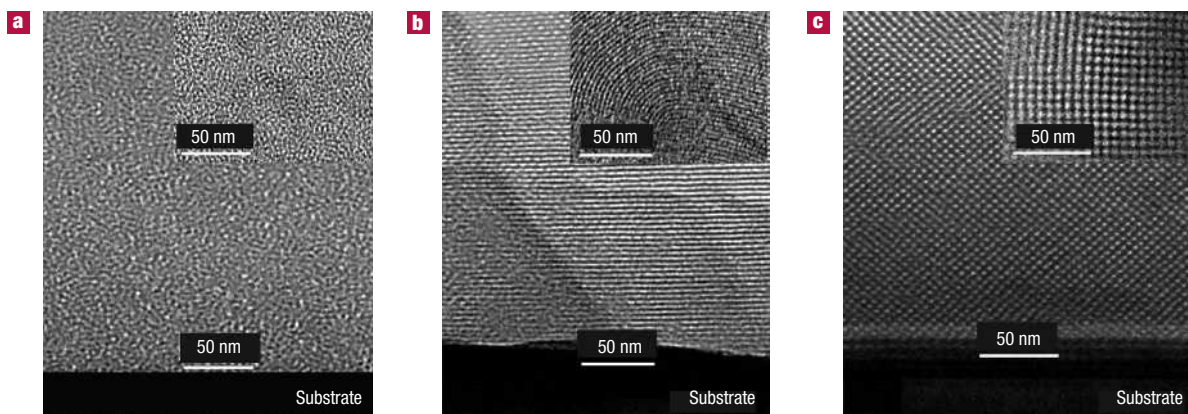


**Figure 2** Cross-sectional and plan-view TEM images. **a**, The disordered (D) nanostructure shows an identical isotropic worm-like morphology in both the cross-sectional and plan-view (inset) images, consistent with a network of interpenetrating cylindrical pores. **b**, The hexagonal (H) nanostructure shows a hexagonal pattern of pores characteristic of the [001] orientation at the top of the cross-sectional image along with a striped pattern, with a repeat distance of around 39.9 Å, characteristic of all other orientations of the cylinders and illustrating their alignment parallel to the substrate surface. Inset: A swirling pattern, indicating lack of orientation within the plane parallel to the substrate (plan-view image). **c**, The cubic (C) nanostructure shows a tetragonal [010] orientation with a repeat distance of 66.2 Å in the cross-sectional image and a highly ordered [100] orientation with a unit-cell parameter of 108 Å in the plan-view image (inset). TEM specimens were made on thinner samples than those for nanoindentation to facilitate cross-sectional TEM sample preparation.

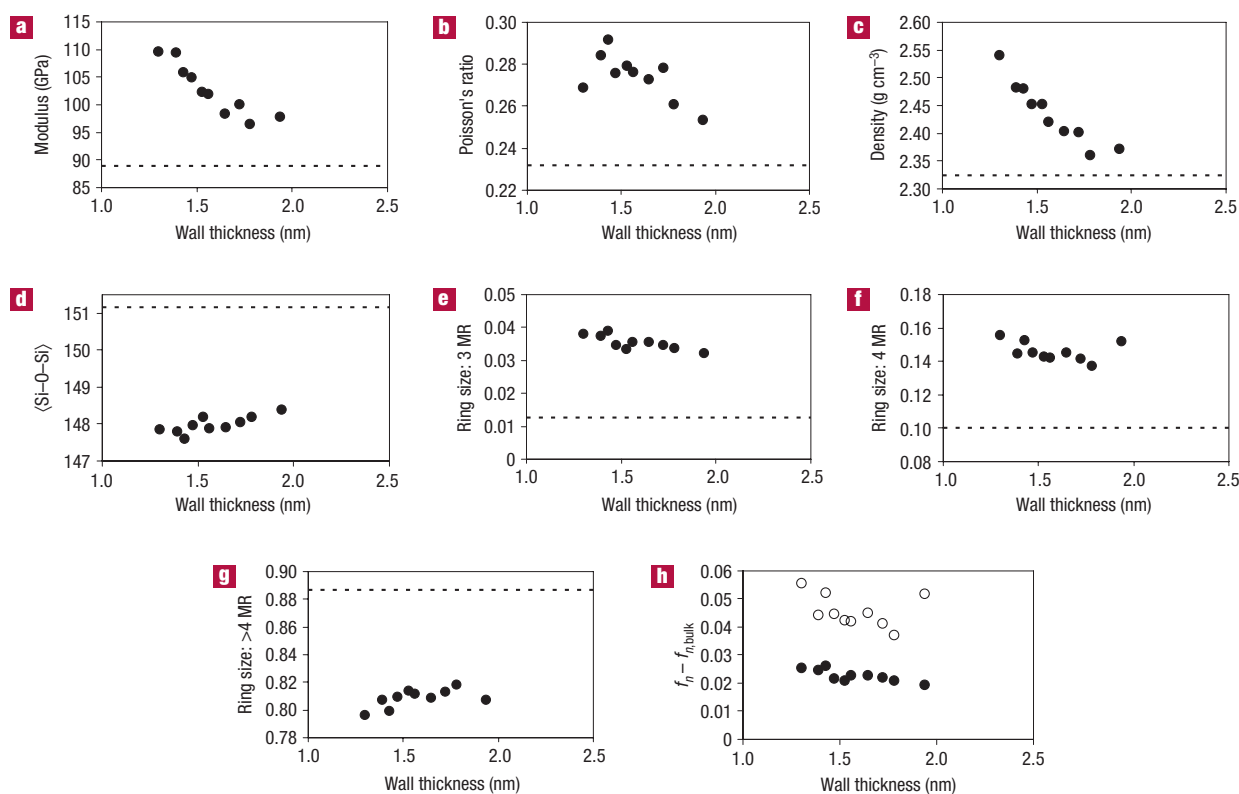


**Figure 3** Simulated trends in mechanical and structural properties of amorphous silica confined to nanometre-scale slabs with thicknesses ranging from 2 to 1 nm. **a-h**, Young's modulus (**a**), Poisson's ratio (**b**), density (**c**), average Si–O–Si bond angle (**d**), fraction of three-membered rings (**e**), fraction of four-membered rings (**f**), fraction of five-membered and larger rings (**g**), excess fractions of three-membered (filled symbols) and four-membered rings (open symbols) (**h**) in nanostructured amorphous silicas over those in the simulated structure of bulk amorphous silica. The dashed lines are the corresponding values simulated for bulk (non-confined) amorphous silica.

and a decrease in the concentration of larger rings (six-membered rings being the most common in bulk amorphous silica). These simulation results are consistent with pressure compaction studies

of silica glass, where compaction (up to 28 GPa) is shown to densify the glass, forming smaller, stiffer three- and four-membered rings at the expense of weaker larger rings, with a concomitant increase

in modulus (by factors of up to 2–3 on the basis of acoustic velocity measurements<sup>22</sup> or molecular simulations<sup>23,24</sup>), although the proportion of small rings revealed by Raman spectroscopy studies<sup>25</sup> is different for pressure-compacted silica than for the nanostructured silica investigated here (see following discussion).

The predicted influence of nanoconfinement on the structure of amorphous silica is confirmed by spectroscopic studies. Figure 4 compares the Raman spectra obtained for H films with those of bulk amorphous silica and a high-surface-area silica xerogel specimen<sup>25</sup> after heating to 200 or 500 °C. Differences in the relative intensities of Raman bands centred at about 600, 490 and 430 cm<sup>-1</sup>, assigned to the decoupled oxygen ring-breathing mode,  $\nu_1(a_g)$ , of three-, four- and five-membered and larger siloxane rings<sup>26,27</sup>, respectively, emphasize that, compared with bulk amorphous silica, the nanostructured sample H has a greater proportion of three- and four-membered rings and a reduced population of larger rings. This difference results in part from the high surface area of the nanostructured sample ( $\sim 1,000 \text{ m}^2 \text{ g}^{-1}$ ), as it is now recognized that dehydroxylation of an amorphous silica surface results in the preferential formation of cyclic trisiloxanes<sup>27</sup>, thereby explaining the high relative intensity of the 600 cm<sup>-1</sup> band—also seen for the high-surface-area silica xerogel (Fig. 4, spectrum 5). However, compared with the xerogel sample, which has a comparable surface area, sample H has a greater population of four-membered rings and fewer larger rings at both 200 and 500 °C (compare spectra 2 and 3; and 4 and 5 in Fig. 4). On the basis of the modelling studies described above, we attribute this to its uniform, ordered nanostructure. Condensation reactions ( $\equiv\text{Si}-\text{OH} + \text{HO}-\text{Si}\equiv \rightleftharpoons \equiv\text{Si}-\text{O}-\text{Si}\equiv + \text{H}_2\text{O}$ , accompanying self-assembly and thermal annealing to 500 °C) confined uniformly within sub-2-nm-thick walls<sup>17,28</sup> lead to an increased population of four-membered rings and a decreased population of larger rings compared with siloxane condensation occurring in high-surface-area silica xerogels, which, owing to their random formation, are typically characterized by a wider range of feature sizes. This conclusion is further confirmed by Raman studies of block-copolymer-templated silicas. Hexagonally ordered SBA-15 powder calcined at 500 °C has a uniform wall thickness close to 3.0 nm (ref. 29) and a substantially greater relative intensity of the 430-cm<sup>-1</sup> band<sup>30</sup> than observed for sample H (spectrum 4).

A reduced average ring size in the uniformly nanostructured specimens is also evident from <sup>29</sup>Si NMR spectroscopy (Fig. 5). For the C, H and D thin-film nanostructures prepared with  $\sim 50\%$  porosity and heated to 500 °C, we see similar, asymmetrically broadened peaks. Statistically acceptable spectral deconvolution shows the samples to be composed of about 1% Q<sup>2</sup>, 26% Q<sup>3</sup> and 73% Q<sup>4</sup> Si species (where Q<sup>*n*</sup> represents the resonance of a silicon atom bonded to *n* 'bridging oxygens' ( $-\text{OSi}\equiv$ ), see Supplementary Information). The average Q<sup>4</sup> chemical shift  $\delta \approx -107 \text{ p.p.m.}$  corresponds to an average Si–O–Si bond angle ( $\phi$ ) of  $\sim 142^\circ$  according to

$$(\delta)(\text{p.p.m.}) = -0.59(\phi) - 23.21 \text{ (ref. 31)}. \quad (3)$$

Modelling and model compound studies<sup>27</sup> indicate  $\phi = 144^\circ$  and  $137^\circ$  for four- and three-membered siloxane rings, respectively, corresponding to  $\delta = -108$  and  $-104 \text{ p.p.m.}$  This explains the observed maxima at about  $\delta = -107 \text{ p.p.m.}$  In comparison, the average Si–O–Si bond angle for bulk amorphous silica is in the range  $\phi = 147^\circ\text{--}151^\circ$  ( $\delta = -110$  to  $-112.5 \text{ p.p.m.}$ ) and SBA-15 powder with a reported wall thickness of about 3 nm has  $\delta = -111$  corresponding to  $\phi = 148.7^\circ$ .

As five-membered and larger rings are puckered, they can accommodate mechanical strain while maintaining the optimum Si–O–Si and O–Si–O bond angles ( $\phi = 148$  and  $\theta = 109.5^\circ$ ,

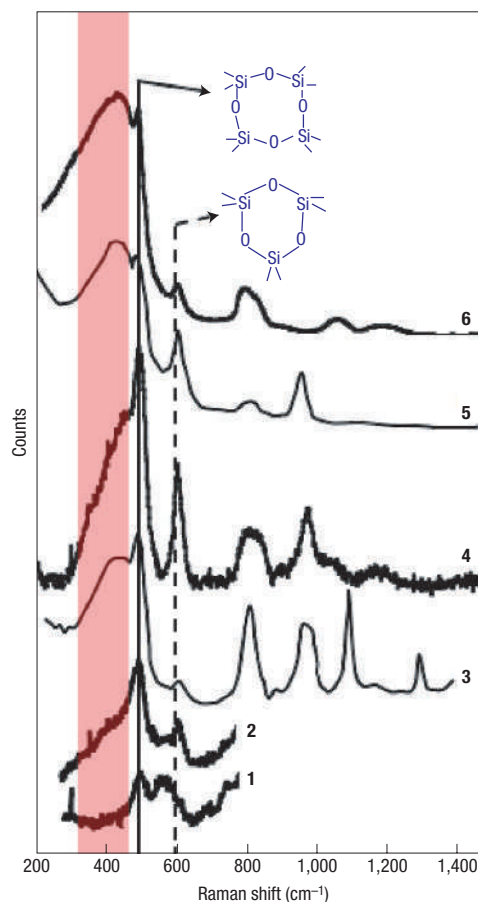


**Figure 4** Raman spectra of self-assembled nanostructured films, a high-surface-area silica xerogel and conventional amorphous silica. 1: H film prepared at room temperature. 2: The same film as in spectrum 1 after heating to 200 °C for 10 min. 3: Silica xerogel after heating to 200 °C (ref. 26). 4: H film prepared by heating the film in spectrum 1 to 500 °C for 10 min. 5: Silica xerogel as in spectrum 3 after heating to 500 °C (ref. 26). 6: Conventional ultrahigh-purity amorphous silica (Infrasil). The  $\sim 490$  and  $600 \text{ cm}^{-1}$  bands are assigned to the symmetric oxygen ring-breathing modes of four- and three-membered siloxane rings (cyclsiloxanes), respectively<sup>27</sup>. The  $\sim 420 \text{ cm}^{-1}$  band is assigned to the symmetric oxygen ring-breathing mode of five-membered and larger cyclic siloxanes<sup>27</sup>. The Raman spectra of the C, H and D thin films were virtually identical.

respectively). Three-membered rings are planar and strained<sup>28</sup>, whereas four-membered rings are nearly planar, requiring that, for three- and four-membered rings, mechanical strain be accommodated by changing the optimum bond angles—deformation of  $\theta$  and reduction of  $\phi$  below  $140^\circ$ , both being very energy intensive<sup>27,32</sup>. This line of reasoning is consistent with the predicted trend of increasing framework modulus with decreasing wall thickness (Fig. 3a)—the increasing population of three- and four-membered rings at the expense of larger, weaker rings causes the framework modulus to exceed that of conventional amorphous silica.

The influence of nanoconfinement on the structure of amorphous silica also serves to explain our anomalous scaling ( $n < 2$  in Fig. 1b). Recent SAXS measurements of calcined mesoporous silicas (templated by non-ionic surfactants as in the present study) showed the wall thickness to decrease progressively (from 1.8 to 1.4 nm) with increasing surfactant

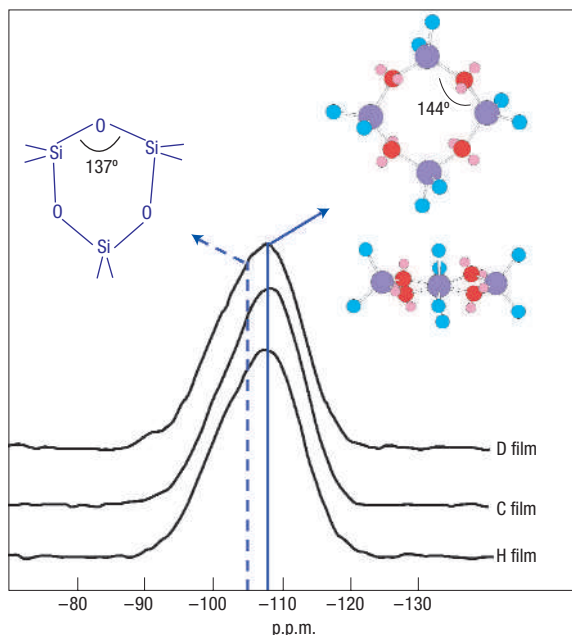


**Figure 5** Solid-state magic-angle-spinning  $^{29}\text{Si}$ -NMR spectra of D, H and C nanostructured silica films prepared by evaporation-induced self-assembly using 5wt% Brij-56 surfactant (as in Fig. 2). The statistically acceptable deconvolution of the peaks indicates a similar extent of siloxane condensation ( $\sim 93\%$ ) for each of the samples (see Table in Supplementary Information), although the films were aged or heat-treated in different manners. This excludes differing extents of framework condensation as being responsible for the hierarchy of film moduli and scaling exponents. The positions of the  $\text{Q}^4$  resonances (silicon centres bonded to four bridging oxygens ( $-\text{O}-\text{Si}$ )) attributable to silicons in three- and four-membered rings were calculated from equation (3), assuming  $\text{Si}-\text{O}-\text{Si}$  bond angles of  $137^\circ$  (ref. 24) and  $144^\circ$  (CS Chem3D Pro software), respectively. Violet circle: Si, red circle: O, cyan circle: H and magenta circle: lone-pair electrons.

concentration/decreasing bulk density<sup>17</sup>. On the basis of our modelling and structural analyses, this in turn should effect a progressive increase in framework modulus. Thus, consistent with our H-S analysis (see the Supplementary Information), scaling exponents  $n < 2$  are explained by the compensatory effect of increasing framework modulus with decreasing bulk density—reducing the sensitivity of  $E$  to bulk density.

H-S analysis can also provide insight into the hierarchy of moduli values at a given density. At a relative density of 0.51, the cubic nanostructure is well modelled by the Schwartz Primitive minimal surface<sup>33</sup>, which is nearly optimal elastically (providing modulus–density scaling close to the H-S upper bound for arbitrary 3D assemblages) and is known to have an effective Poisson's ratio that is consistent with the measured values we report<sup>34</sup>. The 2D hexagonal structure (with axis orientation normal to the indentation direction) has scaling close to the 2D H-S upper bound. At 50% porosity, the ratio of the 3D to 2D upper bounds is about 2, explaining the higher moduli observed for the cubic structures.

We note this trend in modulus may not necessarily correspond to that reported for mechanical stability<sup>11,13</sup>, a test of the sensitivity of the structures to loss of pore volume and surface area resulting from siloxane bond hydrolysis under mechanical compression<sup>35</sup>. In our case, capping of surface silanols with hydrophobic trimethylsilyl groups (see the Methods section) avoids water adsorption and should suppress this type of instability.

It might be anticipated that the disordered worm-like structure would have a modulus intermediate between cubic and hexagonal. However, as its structural coherency and wall thickness cannot be defined by SAXS or TEM, it is not possible to interpret its mechanical response.

Whether self-assembled nanoporous silicas represent a new type of extremal solid is debatable. Self-assembly provides a means to fabricate a nearly optimal 3D cellular architecture<sup>36</sup> and to engineer novel structures and mechanical properties through nanoconfined chemistry. In combination, these attributes lead to unprecedented modulus–density scaling behaviours that improve on those found in natural or larger scale man-made materials.

## METHODS

Thin films were prepared by spin-coating the precursor solutions onto [100] single-crystal silicon wafers or ST-cut piezoelectric crystalline quartz surface-acoustic-wave substrates at a rate of 1,000–2,000 r.p.m. Precursor solutions were prepared by adding a non-ionic surfactant (Brij-56;  $\text{CH}_3(\text{CH}_2)_{15}-(\text{OCH}_2\text{CH}_2)_{10}-\text{OH}$ , Aldrich) to an acidic silica sol prepared from tetraethylorthosilicate [ $\text{Si}(\text{OCH}_2\text{CH}_3)_4$ ] (A2\*\*). The acid concentration used in the A2\*\* synthesis procedure was chosen to minimize the siloxane condensation rate, thereby promoting facile self-assembly during film deposition. In a typical preparation, tetraethylorthosilicate, ethanol, water and dilute HCl (mole ratios: 1:3.8:1.5  $\times 10^{-5}$ ) were refluxed at  $60^\circ\text{C}$  for 90 min. The sol was then diluted with ethanol followed by further addition of water and HCl. Surfactants were added in requisite amounts to achieve initial surfactant concentrations ranging from 0.037 to 0.074 M (3–5 wt%). Spin frequency was used to control film thickness close to  $1\ \mu\text{m}$  to avoid a substrate effect during nanoindentation measurements. The different nanostructures were achieved by different ageing or heat-treatment conditions. Unaged sols resulted in hexagonally ordered films that on rapid heating to  $500^\circ\text{C}$  and holding for 10 min resulted in H films and on slower heating ( $1^\circ\text{C}\ \text{min}^{-1}$  followed by a 3 hr hold) transformed to the C films. Aged sols ( $25^\circ\text{C}$  overnight) resulted in disordered worm-like films that were rapidly heated to  $500^\circ\text{C}$  and held for 10 min. All of the calcined films used for nanoindentation were immediately exposed to 1,1,1,3,3,3-hexamethyldisilazane vapour at  $160^\circ\text{C}$  for 5 min to make the films hydrophobic, thus avoiding the influence of adsorbed water and hydroxyl groups on mechanical properties—notably structural collapse resulting from siloxane bond hydrolysis<sup>11–13,35</sup>.

Thickness and refractive index were determined using a WVASE 32 ellipsometer. The film porosity was calculated from the combined refractive index and surface-acoustic-wave-based nitrogen sorption data. The reduced indentation modulus,  $E_r = E(1 - \nu^2)$ , where  $E$  is Young's modulus and  $\nu$  is Poisson's ratio, was measured at a constant strain rate of  $0.1\ \text{nm}\ \text{s}^{-1}$  using an MTS Nanoindenter XP with a Berkovich pyramidal tip. Ten indents were taken per sample. To mitigate substrate effects, only  $E_r$  values measured at depths between 30–60 nm, where there was no depth dependence, were considered (despite this precaution, nanoindentation is reported to overestimate modulus<sup>37</sup>).  $\nu$  values of 0.23, 0.24 and 0.21 for the D, H and C samples, respectively, were determined directly on thin-film samples from the ratio of compressional and transverse wave velocities measured by an acoustic wave technique (see the Supplementary Information). According to an accurate structure–property formula for the effective elastic moduli of two-phase composites, these experimentally determined effective Poisson's ratios are consistent with corresponding silica framework values that are slightly greater, say roughly between 0.23–0.27 (refs 33,34).

To avoid the timescale issues associated with the slow dynamics in glasses, simulations were carried out on glasses corresponding to inherent structures of equilibrated melts. The van Beest–Kramer–van Santen potential<sup>38</sup> was used for systems composed of 540 atoms and constrained to slabs  $\sim 1$ – $2\ \text{nm}$  thick in one dimension, and infinite in the other two dimensions. Periodic boundary conditions were used in all three dimensions (in the dimension perpendicular to the slab surface, there was a vacuum layer that separated the periodic images of the material). The slabs of silica glass were prepared as follows. First, a molecular dynamics simulation was run at 7,000 K for 25 ps, with an additional potential that constrained the atoms to remain within a slab. Then, the constraining potential was removed, and a molecular dynamics simulation was

run at 3,250 K for 300 ps; during the last 100 ps of this simulation, the structures were saved at 10 ps intervals. From these 10 saved structures, silica glass samples were obtained at zero temperature and zero pressure by minimizing the energy with respect to the atomic positions and the lattice parameters of the simulation cell (note that for silica glass, zero temperature and zero pressure are good approximations to room temperature and atmospheric pressure). The Young's moduli of these silica glass samples were obtained from the second derivatives of the energy with respect to one of the lattice parameters, with the other lattice parameters able to relax. This process was repeated to obtain an ensemble of over 400 silica glass slab samples. Analogous simulations were also carried out for bulk silica.

Received 1 September 2006; accepted 17 April 2007; published 21 May 2007.

## References

- Vincent, J. F. V. & Currey, J. D. *34th Symp. Soc. Exp. Biol.* (Cambridge Univ. Press, Cambridge, 1980).
- Gibson, L. J. The mechanical behaviour of cancellous bone. *J. Biomech.* **18**, 317–328 (1985).
- Gibson, L. J. & Ashby, M. F. The mechanics of three-dimensional cellular materials. *Proc. R. Soc. Lond. A* **382**, 43–59 (1982).
- Hashin, Z. & Shtrikman, S. A variational approach to the theory of the elastic behavior of multiphase materials. *J. Mech. Phys. Solids* **11**, 127–140 (1963).
- Brinker, C. J. & Scherer, G. W. *Sol-Gel Science: The Physics and Chemistry of Sol-Gel Processing* (Academic, San Diego, 1990).
- Woignier, T. & Phalippou, J. Scaling law variation of the mechanical-properties of silica aerogels. *J. Phys.* **50**, C4179–C4184 (1989).
- Miller, R. D. Device physics: In search of low-k dielectrics. *Science* **286**, 421 (1999).
- The International Technology Roadmap for Semiconductors 2005 (ITRS 2005), Interconnect section.
- Lu, Y. F. *et al.* Continuous formation of supported cubic and hexagonal mesoporous films by sol-gel dip-coating. *Nature* **389**, 364–368 (1997).
- Ting, C. Y., Ouyang, D. F. & Wan, B. Z. Preparation of ultra-low dielectric constant porous silica films using Tween 80 as a template. *J. Electrochem. Soc.* **150**, F164 (2003).
- Cassiers, K. *et al.* A detailed study of thermal; hydrothermal; and mechanical stabilities of a wide range of surfactant assembled mesoporous silicas. *Chem. Mater.* **14**, 2317–2324 (2002).
- Gusev, V. Y., Feng, X. B., Bu, Z., Haller, G. L. & O'Brien, J. A. Mechanical stability of pure silica mesoporous MCM-41 by nitrogen adsorption and small-angle X-ray diffraction measurements. *J. Phys. Chem.* **100**, 1985–1988 (1996).
- Hartmann, M. & Bischof, C. Mechanical stability of mesoporous molecular sieve MCM-48 studied by adsorption of benzene; n-heptane; and cyclohexane. *J. Phys. Chem. B* **103**, 6230–6235 (1999).
- Wu, J. J., Liu, X. Y. & Tolbert, S. H. High-pressure stability in ordered mesoporous silicas: Rigidity and elasticity through nanometer scale arches. *J. Phys. Chem. B* **104**, 11837–11841 (2000).
- Kirsch, B. L., Chen, X., Richman, E. K., Gupta, V. & Tolbert, S. H. Probing the effects of nanoscale architecture on the mechanical properties of hexagonal silica/polymer composites thin films. *Adv. Funct. Mater.* **15**, 1319 (2005).
- Fan, H. Y. *et al.* Rapid prototyping of patterned functional nanostructures. *Nature* **405**, 56–60 (2000).
- Smarsly, B., Gibaud, A., Ruland, W., Sturmayer, D. & Brinker, C. J. Quantitative SAXS analysis of oriented 2D hexagonal cylindrical silica mesostructures in thin films obtained from nonionic surfactants. *Langmuir* **21**, 3858 (2005).
- Frye, G. C. *et al.* in *Better Ceramics Through Chemistry IV* (eds Zelinski, B. J. J., Brinker, C. J., Clark, D. E. & Ulrich, D. R.) 583–593 (Mater. Res. Soc., San Francisco, 1990).
- Oliver, W. C. & Pharr, G. M. An improved technique for determining hardness and elastic-modulus using load and displacement sensing indentation experiments. *J. Mater. Res.* **7**, 1564–1583 (1992).
- Jain, A. *et al.* Effects of processing history on the modulus of silica xerogel films. *J. Appl. Phys.* **90**, 5832–5834 (2001).
- Jiang, Y.-B., Liu, N., Gerung, H., Cecchi, J. L. & Brinker, C. J. Nanometer-thick conformal pore sealing of self-assembled mesoporous silica by plasma-assisted atomic layer deposition. *J. Am. Chem. Soc.* **128**, 11018–11019 (2006).
- Zha, C. S., Hemley, R. J., Mao, H. K., Duffy, T. S. & Meade, C. Acoustic velocities and refractive-index of SiO<sub>2</sub> glass to 57.5-GPa by Brillouin-scattering. *Phys. Rev. B* **50**, 13105–13112 (1994).
- Lacks, D. J. Localized mechanical instabilities and structural transformations in silica glass under high pressure. *Phys. Rev. Lett.* **80**, 5385–5388 (1998).
- Lacks, D. J. First-order amorphous-amorphous transformation in silica. *Phys. Rev. Lett.* **84**, 4629–4632 (2000).
- Sugiura, H., Ikeda, R., Kondo, K. & Yamadaya, T. Densified silica glass after shock compression. *J. Appl. Phys.* **81**, 1651–1655 (1997).
- Brinker, C. J., Kirkpatrick, R. J., Tallant, D. R., Bunker, B. C. & Montez, B. NMR confirmation of strained defects in amorphous silica. *J. Non-Cryst. Solids* **99**, 418–428 (1988).
- Galeener, F. L. in *The Structure of Non-Crystalline Materials* (eds Gaskell, P. H., Parker, J. M. & Davis, E. K.) 337–359 (Taylor and Francis, London, 1982).
- Gibaud, A. *et al.* Wall thickness and core radius determination in surfactant templated silica thin films using GISAXS and X-ray reflectivity. *Europhys. Lett.* **63**, 833 (2003).
- Trofymuk, O., Levchenko, A. A., Tolbert, S. H. & Navrotsky, A. Energetics of mesoporous silica: Investigation into pore size and symmetry. *J. Phys. Chem. B* **17**, 3772–3783 (2005).
- Borodko, Y. *et al.* Structure sensitivity of vibrational spectra of mesoporous silica SBA-15 and Pt/SBA-15. *J. Phys. Chem. B* **109**, 17386–17390 (2005).
- Oestrike, R. *et al.* High-resolution Na-23; Al-27; and Si-29 NMR-spectroscopy of framework aluminosilicate glasses. *Geochim. Cosmochim. Acta* **51**, 2199–2209 (1987).
- O'Keefe, M. & Gibbs, G. V. Defects in amorphous silica: Ab initio MO Calculations. *J. Chem. Phys.* **81**, 876 (1984).
- Torquato, S. & Donev, A. Minimal surfaces and multifunctionality. *Proc. R. Soc. Lond. A* **460**, 1849–1856 (2004).
- Torquato, S. Effective stiffness tensor of composite media: II. Applications to isotropic dispersions. *J. Mech. Phys. Solids* **46**, 1411–1440 (1998).
- Tatsumi, T., Koyano, K., Tanaka, Y. & Nakata, S. Mechanochemical collapse of M41S mesoporous molecular sieves through hydrolysis of siloxane bonds. *Chem. Lett.* 469–470 (1997).
- Torquato, S., Donev, A., Evans, A. G. & Brinker, C. J. Manufacturable extremal low-dielectric, high-stiffness porous materials. *J. Appl. Phys.* **97**, 124103 (2005).
- Alud, B. *Acoustic Fields and Waves in Solids* (Wiley, New York, 1973).
- Van Beest, B. W. H., Kramer, G. J. & van Santen, R. A. Force-fields for silicas and aluminophosphates based on ab initio calculations. *Phys. Rev. Lett.* **64**, 1955 (1990).

## Acknowledgements

We thank D. Doshi (UNM), A. Gibaud (Université du Maine), B. Smarsly (Max Planck Institute of Colloids and Interfaces) and R. Köhn (Munich) for GISAXS and SRSAXS, N. Liu (UNM) for molecular simulations of the cyclo-tetrasiloxane and G. Scherer (Princeton University) for many useful discussions. This work was supported by the US Department of Energy Office of Science, Air Products and Chemicals, Incorporated, Sematech, the US Air Force (FA9550-04-1-0087-CJB; F49620-03-1-0406-ST), the Army Research Office (DAAD19-03-1-0227-CJB), NSF (0402867-DJL) and the University of New Mexico/Rutgers/NSF Ceramics and Composites Research Center. TEM investigations were carried out in the Department of Earth and Planetary Sciences at the University of New Mexico. Sandia is a multiprogram laboratory operated by Sandia Corporation, a Lockheed-Martin Company, for the US DOE. Correspondence and requests for materials should be addressed to C.J.B. Supplementary Information accompanies this paper on [www.nature.com/naturematerials](http://www.nature.com/naturematerials).

## Author contributions

H.F. prepared the nanostructured silicas, devising the means to achieve three different architectures at each density, carried out TEM and other structural characterization and oversaw the experimental work. C.H. under the guidance of T.B. carried out the nano-indentation experiments. R.S. and D.T. carried out Raman spectroscopy on thin-film nanostructures and (earlier) bulk silica gels. R.A. carried out <sup>29</sup>Si magic-angle-spinning NMR spectroscopy. D.J.K. developed acoustic means to measure Poisson's ratio of thin-film samples. D.J.L. carried out molecular simulations. S.L. carried out theoretical analyses of modulus–density scaling relationships. C.J.B. directed the research and contributed to the interpretation of the combined experimental, modelling and theoretical studies.

## Competing financial interests

The authors declare no competing financial interests.

Reprints and permission information is available online at <http://npg.nature.com/reprintsandpermissions/>